LRP 633/99 April 1999

Energy Confinement and MHD Activity in Shaped TCV Plasmas with Localised Electron Cyclotron Heating

A. Pochelon, T.P. Goodman,
M. Henderson et al.

accepted for publication in

NUCLEAR FUSION

IAEA 1998, Yokohama Special Issue

ISSN 0458-5895

ENERGY CONFINEMENT AND MHD ACTIVITY IN SHAPED TCV PLASMAS WITH LOCALISED ELECTRON CYCLOTRON HEATING

A. POCHELON, T.P. GOODMAN, M. HENDERSON, C. ANGIONI, R. BEHN, S. CODA, F. HOFMANN, J-P. HOGGE, N. KIRNEVA**, A.A. MARTYNOV**, J-M. MORET, Z.A. PIETRZYK, F. PORCELLI*, H. REIMERDES, J. ROMMERS, E. ROSSI*, O. SAUTER, M.Q. TRAN, H. WEISEN, S. ALBERTI, S. BARRY, P. BLANCHARD, P. BOSSHARD, R. CHAVAN, B.P. DUVAL, Y.V. ESIPCHUCK**, D. FASEL, A. FAVRE, S. FRANKE, I. FURNO, P. GORGERAT, P-F. ISOZ, B. JOYE, J.B. LISTER, X. LLOBET, J-C. MAGNIN, P. MANDRIN, A. MANINI, B. MARLETAZ, Ph. MARMILLOD, Y. MARTIN, J-M. MAYOR, J. MLYNAR, Ch. NIESWAND, P.J. PARIS, A. PEREZ, R.A. PITTS, K.A. RAZUMOVA**, A. REFKE, E. SCAVINO, A. SUSHKOV**, W. VAN TOLEDO, G. TONETTI, F. TROYON, P. VYAS.

Centre de Recherches en Physique des Plasmas,
Association EURATOM - Confédération Suisse
Ecole Polytechnique Fédérale de Lausanne
CH-1015 Lausanne, Switzerland

*Istituto Nazionale Fisica della Materia and Department of Energetics
Politecnico di Torino
I-10129 Torino, Italy

**Institute of Nuclear Fusion, Russian Research Centre,
Kurchatov Institute
RF-123182 Moscow, Russia

Abstract

Confinement in TCV (Tokamak à Configuration Variable) electron cyclotron heated discharges is studied as a function of plasma shape, i.e. as a function of elongation $1.1 < \kappa < 2.15$ and triangularity $-0.65 \leq \delta \leq 0.5$. The electron energy confinement time is found to increase with elongation, in part due to the increase of plasma current with elongation. The beneficial effect of negative triangularities is most effective at low power and tends to reduce at the higher powers used.

The large variety of sawtooth types observed in TCV for different power deposition locations from on axis to the q=1 region can be simulated with a model including a local power deposition, a growing m/n=1 island (convection and reconnection), plasma rotation and finite heat diffusivity across flux surfaces. Furthermore, a model with local magnetic shear reproduces the experimental observation that the sawtooth period is at maximum when the heating becomes close to the q=1 surface.

1. INTRODUCTION

The improvement in tokamak performance over the last 25 years is not only due to the fact that tokamaks have grown in size, but is also a result of modifications of the basic tokamak concept. The evolution from circular to noncircular cross sections and, in particular, the vertical elongation of the plasma cross section κ allows for higher plasma current, since the maximum current scales typically as $I_p \sim (\kappa^2+1)/2$.

Increasing the plasma current offers two advantages. The first advantage is that the global energy confinement time increases nearly linearly with current, according to several widely used scaling laws, in L confinement mode as in H mode [1, 2, 3]. The second advantage is that vertically elongated and D-shaped cross sections allow much higher normalised pressures, i.e. β values, than circular ones [4, 5]. The β-limit, determined from numerical MHD stability analysis [5], $\beta(\%) = c_T I_p(\mathrm{MA})/[a(\mathrm{m})B(\mathrm{T})]$, scales with the plasma current I_p; a is the minor radius, B the toroidal magnetic field, and c_T is the Troyon factor, which is typically between 2.5 and 4.0, depending on the pressure and current profiles. The good agreement of ideal β-limit calculations in highly elongated plasmas with experiment [6, 7] strongly suggests to increase the design κ in ITER.

Electron Cyclotron Heating [8, 9] (ECH) experiments on TCV (achieved parameters: R=0.89m, a=0.25m, κ=2.58, -0.7<δ<0.9, I_p=1MA, B=1.43T) are presently aimed at the study of the confinement properties of variably shaped plasmas. For these studies, an ECH power of 1.4 MW is injected at the second harmonic, 82.7GHz. This power level is already an order of magnitude larger than the Ohmic power during ECH, but represents only a third of the planned total power (3MW at the second harmonic and 1.5MW at the third harmonic, 118 GHz). EC heating has been chosen for TCV, to cope with the large variety of plasma shapes. Each 0.5 MW gyrotron is connected to a steerable launcher, which can be moved during a tokamak discharge. A universal polariser is included in each transmission line to provide the polarisation needed at the plasma boundary for optimal power coupling.

A number of improvements have been made to the first wall graphite protection during the 1997 shutdown. Surface coverage has been increased from ~60% to ~90% by addition of new tiles on previously exposed areas on the low field side wall. These new elements now allow for heating of negative triangularity discharges. The central column tiles have been completely redesigned and have now a toroidal profile optimised for high power experiments. The wall is boronised regularly.

2. CONFINEMENT AS A FUNCTION OF PLASMA SHAPE

2.1 Confinement study: definition and parameter range

The aim is to study confinement as a function of elongation κ, (1.1 < κ < 2.15), and triangularity δ, (-0.65<δ<0.55), both values defined at the edge. Two values of q_{cng} ($q_{cng}=5abB/RI_p$), 1.7 and 3 are used, (2.3<q_a<6; 0.2<I_p<0.7MA). The engineering safety factor q_{cng} is used instead of the usual q_a to parametrise the plasma current since constant q_{cng} results in similar normalised profiles independent of the plasma shape [10]. The standard central density n_{eo} is ~2-2.5×10^{19} m^{-3}, while the influence of density is only studied for a restricted number of shapes. All discharges are limited L-mode discharges. Up to 1.4 MW ECRH was injected, with the power deposition region located near the magnetic axis, largely inside the sawtooth inversion radius. At higher q_{cng}, due to finite beam width and shrinking of the q=1 surface, together with a smaller paramagnetic resonance shift at lower current, the beam moves somewhat off-axis, but is still well inside the q=1 radius. Thus, we have always central power deposition conditions.

Three gyrotrons were used for this study, two of them launching from the upper lateral ports and one from the equatorial port. The power was raised to its maximum value in three steps of typically 0.2 s duration. Confinement data are used after the establishment of a constant soft X-ray flux, which led to the exclusion of a 40-50 ms transient period at the start of each power step. Between the 2nd and 3rd step the power was modulated during 0.2 s. The power deposition location was obtained from soft X-rays at the EC shut-off [11], from power modulation experiments, and qualitatively from the sawtooth shapes (see section 3.1).

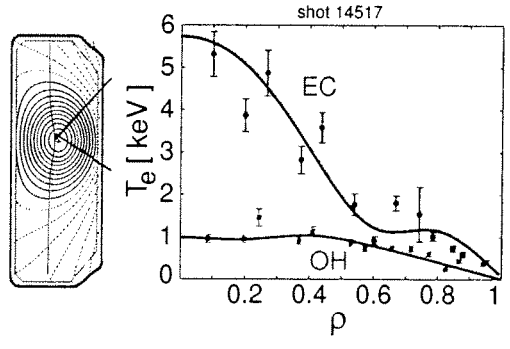

FIG. 1. Thomson electron temperature profile for κ=1.5, δ=0.2, n_{eo}=1.3×10^{19} m^{-3} during Ohmic and ECRH (1.4 MW). Central deposition, inside the q=1 surface, in blue, is aimed with upper lateral and equatorial beams.

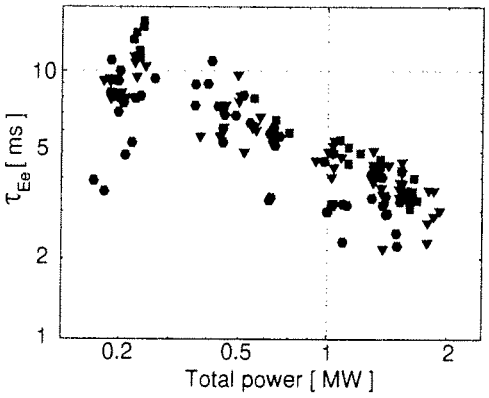

FIG. 2. Electron confinement time versus total power for κ=1.5, δ=0.2 (red squares: n_{eo19}>3, green triangles: 2<n_{eo19}<3, blue hexagons: n_{eo19}<2).

The EC power, P_{EC}, can be measured near the torus calorimetrically between discharges. The gyrotron power can be set within 5% and is indeterminate to ±10%.

The electron energy content W_{Ee} is obtained from Thomson scattering measurements, taken every 17 ms. The T_e and n_e profiles, measured along a vertical chord (at R=0.9m), are projected onto normalised flux co-ordinates and fitted with cubic splines. Therefore the calculation of W_{Ee} depends on the equilibrium reconstruction and on the profile fits. This procedure is straightforward for positive triangularity and low elongation discharges, where MHD mode activity is low, as for the case of the discharge shown in Fig. 1. For negative triangularity and high elongation, the profiles show occasionally large fluctuations within the sawtooth inversion radius, which can make the fitting procedure problematic. Such shots had so far to be rejected from the database. The electron energy sometimes fluctuates strongly in time owing to large sawtooth relaxations at positive triangularity and with 1.4 MW of ECRH. Typically ten Thomson profiles were available after the exclusion of the initial transient period at the beginning of each step. These multiple profiles were averaged to reduce the influence of fluctuations.

Typical values of the effective charge Z_{eff}, calculated from soft X-ray flux (dominated by carbon emission) and Thomson temperatures, are $Z_{eff} \geq 4$ during the Ohmic and ECRH phases. Bulk ion temperatures from neutral particle analysis range from 200 to 250 eV. Therefore the ion contribution to the total energy is negligible.

2.2 MHD activity

MHD activity does not only influence the T_e profile reconstruction but can also degrade the confinement itself. In particular for $\delta < -0.2$ the m/n=2/1 mode has been frequently observed during phases with and without auxiliary heating power and irrespective of the edge safety factor.

Sawteeth were present in a wide range of the investigated plasma shapes. Ohmic sawteeth, at κ=1.5, δ=0.2 and typical densities of 2-3×10^{19}m^{-3} have a period $\tau_{ST} \sim 2$ ms. Their period and size increase with triangularity up to $\tau_{ST} \sim 3$ ms and up to a relative crash amplitude of 20% observed with a soft X-ray diode viewing the plasma core ($I_{SX\text{-}R}$). For negative δ the relative crash amplitude decreases down to a few % and can disappear within the resolution limit [12]. The crash amplitude as well as the sawtooth period decrease with increasing elongation. Occasionally, no sawteeth have been observed in discharges with $\kappa > 2$.

With the addition of ECH, deposited within the q=1 surface, different forms of sawteeth have been observed, ranging from normal triangular sawteeth for on-axis deposition to saturated and inverted sawteeth for deposition closer to the inversion radius. For q_{eng}=2, κ=1.5, δ=0.2, the observed sawtooth shapes change with increasing heating power from normal to saturated to inverted sawteeth. For higher q_{eng}=3, therefore with a reduced inversion radius, saturated sawteeth already appear at lower heating power, indicating that the actual deposition was relatively somewhat further off-axis, closer to the inversion surface (see section 3.1.1).

The effect of power on sawtooth period and size indicates a strong triangularity dependence: for instance at moderate elongation $\kappa \sim 1.5$, for small positive triangularity $\delta > 0.2$ and at low q_{eng} to ensure central deposition, the sawtooth period and crash amplitude increase with increasing heating power up to $\tau_{ST} \sim 5$ ms and up to a relative crash amplitude of 35%, whereas for $\delta < 0.2$ the sawtooth period decreases with increasing heating power, with smaller relative crash amplitude. Therefore, with increasing power, positive triangularity shows a sawtooth stabilisation effect, but associated with large crash amplitudes; on the contrary, increasing power in negative triangularity discharges induces sawtooth destabilisation and relative smaller crash amplitudes, which can be of advantage in schemes trying to avoid seed island formation.

2.3 Scaling of electron energy confinement time

The dependence of the electron energy confinement time on total power and density was studied over a wide power range for the different plasma shapes and in particular in the centre of the (κ,δ) scan (κ=1.5, δ=0.2), as shown in Fig. 2. The electron energy confinement time is clearly seen to decrease with power and to increase with density.

In an attempt to obtain a simple general power law to describe the dependence of the electron confinement time τ_{Ee} on average line density n_{e_av}, total power P, edge elongation κ, edge triangularity δ and plasma current I_p, we have applied a multi-variable regression to the database. The dependence's on κ and I_p cannot be separately determined, owing to the strong correlation between these quantities in our data set. The power law we are able to express so far must therefore contain a free parameter, as follows:

$$\tau_{Ee}[\mathrm{ms}] = 2 \times 6^{\alpha_I}\, n_{e\_av19}{}^{\alpha_n} P^{\alpha_P} I_p{}^{\alpha_I} \kappa^{\alpha_\kappa} (1+\delta)^{\alpha_\delta}\ [\mathrm{m}^{-3}, \mathrm{MW}, \mathrm{MA}], \qquad (1)$$

where α_n=0.46±0.2, α_P=-0.7±0.1, α_δ=-0.35±0.3, α_κ=1.4(1-α_I)±0.4 and α_I remains undetermined. These uncertainties result from a 25% error on τ_{Ee}. Good fits are obtained with α_I in the range $0 \le \alpha_I \le 0.7$, as illustrated in Fig. 3 for the case $\alpha_I = 0.5$.

If instead of the above five variable regression a four variable regression is used, with no explicit current dependence (α_I=0), a very favourable elongation power exponent, α_κ~1.4, is obtained, indicating the good overall effect of elongation, leaving off the determination of the separate contribution of elongation and plasma current. In fact, further data at moderate elongation are needed to reduce the strong correlation of plasma current and elongation in the present database. It can be noted however that the main reason to develop elongated discharges is to increase the plasma current. At high elongation, low current operation is limited by vertical stability, in Ohmic heated discharges and in the present central deposition ECRH cases. Therefore, broadening of the current profile by proper use of off-axis ECRH or ECCD could also be of help to decorrelate elongation and current by enlarging the range of stable equilibria.

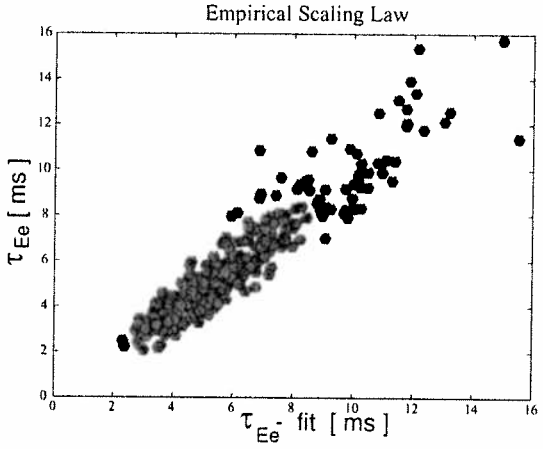

FIG. 3. Empirical scaling law for TCV ECRH data set, see equation (1), in the case of α_I = 0.5.

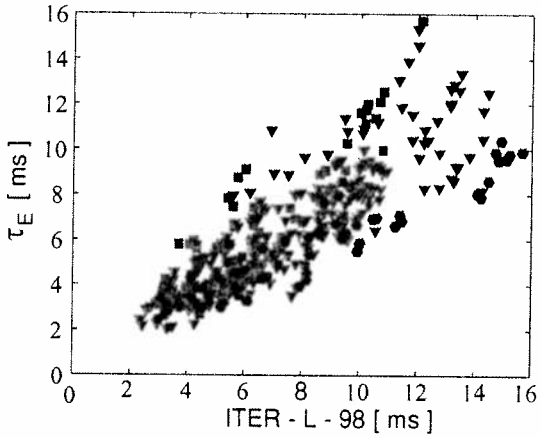

FIG. 4. Fit to ITER-98-L mode scaling law. Since triangularity does not appear in ITER-98-L, it is explicitly indicated by the symbols: negative δ appear favourable (red squares: δ<0, green triangles: 0<δ<0.3, blue hexagons: δ>0.3).

The scaling (1) displays qualitative similarities with recent scaling laws, such as the ITER-98-L mode scaling [2], where α_n=0.40, α_P=-0.73, α_I=0.96, α_κ=0.64. Clearly, the α_n and α_P exponents are in agreement, within the uncertainties, with our scaling; however, α_κ and α_I are not both compatible with our scaling. Plotting our data against ITER-98-L, as shown in Fig. 4, shows the beneficial effect of negative triangularities.

The constraints α_n=1/2 and α_P=-2/3 from the ELMy H-mode ITER data base [3] are also compatible with our scaling. The fit to this ELMy H-mode scaling, shown in Fig. 5, indicates again the beneficial effect of negative triangularities.

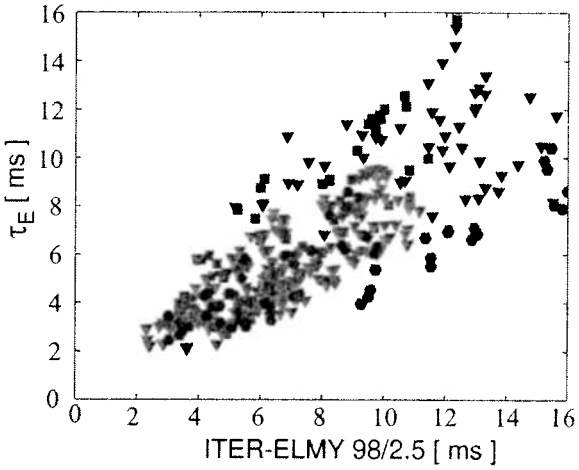

FIG. 5. Fit to ELMy-H-mode scaling law with H-factor = 2.5 [3]. Same symbols as in Fig. 4.

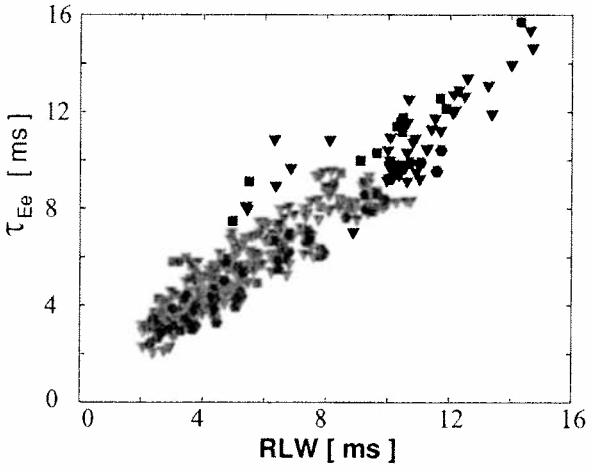

FIG. 6. Fit to Rebut-Lallia-Watkins scaling law. Negative δ appear favourable. Same symbols as in Fig. 4.

Naturally, such a general scaling, being based on the entire data set, may overlook more detailed effects in particular regions of the parameter space. For instance, the degradation of confinement with power, when studied discharge by discharge, using the different power steps in one discharge (maintaining constant current and plasma shape), becomes progressively more pronounced as density is increased. Also, the beneficial effect of low triangularity or slightly negative triangularity appears to be stronger at low total power.

Most of the improvement of confinement time with shape changes in Ohmic plasmas had been explained earlier in terms of geometrical effects. However, the thermal conductivity of ohmic plasmas was found to be independent of the plasma shape. This observation, combined with geometrical effects on the temperature gradient and degradation with increasing energy flux, was able to explain the observed variation in the energy confinement time [13].

The TCV confinement time is plotted against the Rebut-Lallia-Watkins confinement scaling [14] in Fig. 6 for comparison and shows good agreement. Since the RLW scaling contains no triangularity dependence, the data points have again been subdivided into three triangularity classes, which shows the beneficial effect of negative triangularity, although less visibly than in scalings of Fig. 4 and 5. The best fit is obtained with RLW, but the two others are not far off.

2.4 Transport modelling (PRETOR, ASTRA)

Some of the EC heated discharges have been simulated using the transport code PRETOR [15]. PRETOR is a predictive time-dependent transport simulation code for tokamaks: it couples a 2-D equilibrium solver with the flux-surface averaged 1-D transport equations to compute the evolution of temperature and density of electrons, ions and impurities. The RLW model [14], which is implemented in the code, has been modified, only in its geometrical dependence, to simulate discharges with an edge safety factor larger than 5, as the original model did not allow satisfactory simulations of Ohmic TCV discharges in this domain [16]. The experimental temperature profiles of a single shot in the ohmic phase have been analysed and the heat conductivity has been adjusted to reproduce the experimental behaviour, which implies a relatively large transport at the edge and smaller in the centre. The formula of the electron thermal conductivity χ_{RLW} in [16] was changed to:

$$\chi_{RLW} = \frac{0.45}{\sqrt{R_0}}\sqrt{\varepsilon}\sqrt{1+Z_{eff}}\left|\left(\frac{\partial_\rho T_e}{T_e}+2\frac{\partial_\rho n_e}{n_e}\right)\frac{q^2}{\partial_\rho q}\right|\sqrt{\frac{T_e}{T_i}}B_t^{-1} \left(\frac{1}{2}+\frac{\rho}{a}\right)^2\left(1-\frac{\left(\partial_\rho T_e\right)_c}{\partial_\rho T_e}\right)H\left(\partial_\rho T-\left(\partial_\rho T_e\right)_c\right) \quad (2)$$

where H(x) is the Heaviside function, $\partial_\rho = \partial / \partial\rho$, and $(\partial_\rho T_e)_c$ is the electron temperature critical gradient.

With this model, keeping fixed the free parameter in all the transport coefficients, discharges have been simulated in the Ohmic and in the ECH phases. A satisfactory agreement is obtained for the temperature, Fig. 7 a), and density profiles, Fig. 7 b), the electron thermal energy and the confinement time, assuming total absorption for the different ECH powers injected. In some ECH discharges a "pump-out" effect is observed in between sawtooth crashes, which implies that the local particle transport coefficients should be modified in the centre. This has not yet been included in PRETOR but is not significant on the confinement time.

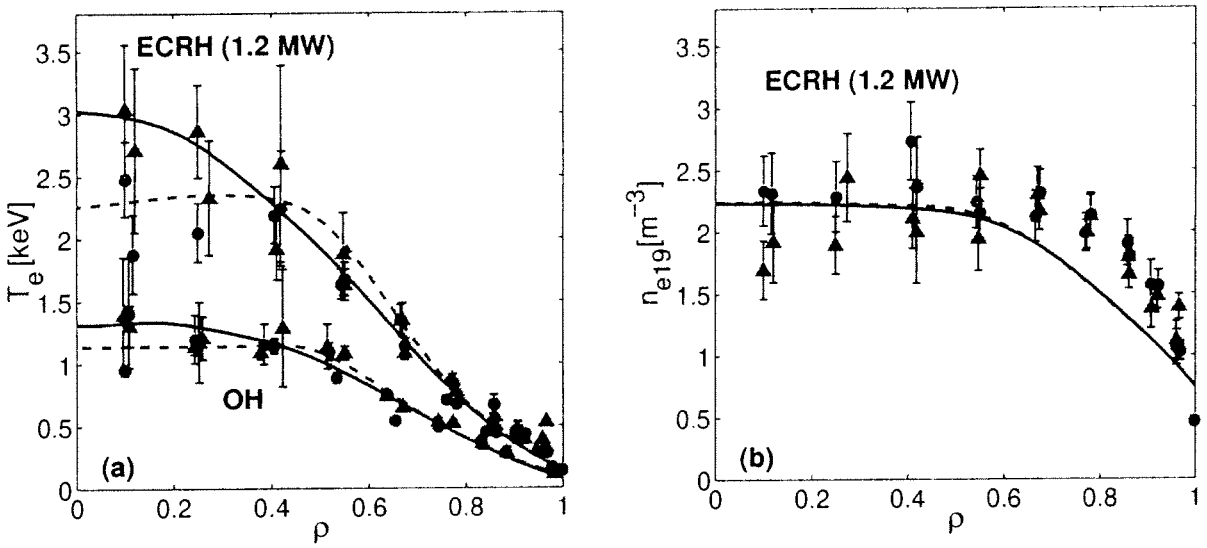

FIG. 7. Comparison between PRETOR temperature (a) and density profiles (b) and TCV experimental profiles in Ohmic and ECR heated (1.2 MW) discharges, before (blue solid line and triangles) and after (red dashed line and solid circles) sawtooth crash (κ=1.8, δ=0.2, $n_{e0}=2.3\times10^{19}m^{-3}$, q~5). Due to central pump-out with central power deposition, the experimental density profile becomes hollow in such a shot and fills in at each sawtooth crash; the Ohmic density profile - not shown - is close to the after crash ECH profile.

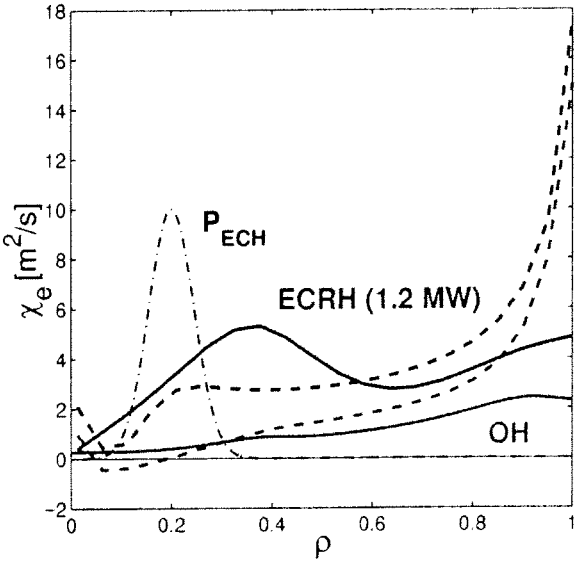

FIG. 8. Comparison between PRETOR (solid lines) and ASTRA (dashed lines) χ_e profiles in Ohmic (red lines) and ECH discharges (blue lines). The dash-dotted line indicates the ECH power deposition profile [a.u.].

Simulating the same discharge with ASTRA, a transport code based on the canonical transport model [17], a model of self-consistent profiles including a heat pinch, good agreement is also found with temperature profiles and confinement time. With a measured ratio of P_{rad}/P_{OH}~0.2, using the radiated power measured from bolometry, one must assume 90% absorption of injected power, which within the error bar of the power measurement. A higher radiation level, around P_{rad}/P_{OH} ~0.3, would be consistent with full power absorption. Thus our data can satisfactorily be simulated by both transport codes.

Comparing the heat diffusivities χ_e obtained from the ASTRA and PRETOR codes in Fig. 8, we can observe that: 1) ASTRA shows a larger transport enhancement close to the edge, 2) there is good agreement in the intermediate region $0.5 < \rho < 0.8$, with χ_e's in ASTRA higher than PRETOR by about 20% in ECRH, by a factor 2 in Ohmic, 3) inside $\rho = 0.5$, ASTRA shows the effect of heat pinch, which can allow for inward total heat fluxes at the centre. On the other hand, PRETOR shows a consistent enhancement of the anomalous transport close to the ECRH power deposition location caused by the presence of steeper temperature gradients.

3. SIMULATION OF CENTRAL RELAXATIONS WITH LOCALISED POWER DEPOSITION

3.1 Central relaxation shape modelling

3.1.1 Experimental description

Non-standard sawtooth traces have been observed in TCV during intense localised EC heating [18]. Fig. 9 shows a sequence of soft X-ray traces obtained while varying the ECH deposition radius. With on-axis deposition, standard, i.e. triangular, sawteeth are observed. However, as the ECH absorption region is moved off-axis, the soft X-ray traces change their shape: partially saturated and saturated sawteeth are observed when the heating is still within the $q=1$ radius. Interestingly, the precursor oscillations that precede the fast relaxation phase of a saturated sawtooth sometimes double their frequency [19]. Humpback sawteeth, first reported by the T-10 team [20], are observed in TCV when the heat is deposited close to the inversion radius. For slightly larger deposition radii, the soft X-ray traces acquire hill-like shapes of low amplitude. Another intriguing experimental observation concerns the optimal deposition radius for obtaining high central temperatures: this radius appears to be often close to the q=1 radius. In fact, the sawtooth or humpback period is longest in this case, and the confinement time is as large as for central deposition.

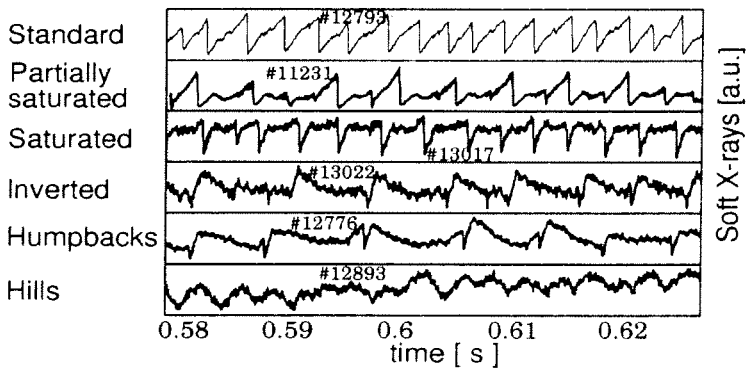

FIG. 9. Standard sequence of central relaxations obtained when moving deposition from magnetic axis (top) to inversion radius (bottom). Standard sawteeth are produced by on-axis power deposition, humpbacks and hills by deposition close to sawtooth inversion radius.

3.1.2 Model of a growing island under localised heating and diffusion

A theoretical model has been recently developed, which accounts for many of the observed features [21]. The model is based on the combined effects of m/n=1 magnetic island dynamics, localised EC heating, finite heat diffusivity across the magnetic field lines and plasma rotation. According to this model, the flux surfaces acquire a distinct m/n=1 topology in the plasma central region, described by a helical flux function, $\psi_*\left[r, \vartheta - \varphi, \xi(t)\right]$, whose detailed analytic form is given in Ref. [21]. Here, $\xi(t) \approx w(t)/2$ is the displacement of the magnetic axis as a consequence of the excitation of a resistive internal kink mode and $w(t)$ is the m/n=1 magnetic island width. The time evolution of $\xi(t)$ is not predicted theoretically, but it can be inferred from the experimental data. The limit $\xi(t) \to \rho_{mix}$, with ρ_{mix} the Kadomtsev mixing radius [22], corresponds to full

reconnection. Nevertheless, the model is applicable as well to cases of partial sawtooth reconnection.

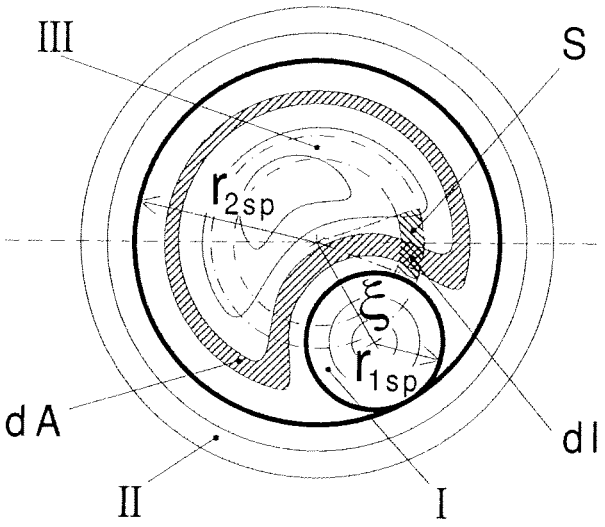

FIG. 10. Heat deposition and distribution in a growing and rotating m=1 island.
Regions: I) Displaced core, vanishing at full reconnection, II) Outer region, III) Growing island region with new magnetic axis.
The heat deposited in the elemental surface dl of the heat source S spreads over the crescent shaped hatched area by parallel diffusion. The addition of rotation further distributes the heat along other families of flux surfaces.

An example of $\psi_* = const$ contour lines for a given $\xi(t)$ is shown in Fig. 10. The deposited thermal energy spreads rapidly and uniformly on flux surfaces because of the large (practically infinite) parallel thermal conductivity. Rotation distributes the deposited heat on several flux tubes intersecting the ECH absorption region (for the sake of simplicity, we assume rigid toroidal rotation). With reference to Fig. 10, if we denote by dA the cross-sectional area of a generic flux tube and with dl its intersection with the heated region, we can write the ECH power density averaged over flux surfaces as $\langle S \rangle(A) = \rho \partial l / \partial A$, where $\rho = P_{ECH} / V_H$ (= *const* for simplicity) is the power density, P_{ECH} is the total ECH absorbed power and V_H is the absorption volume. Note that the thermal energy is transported radially by parallel heat diffusion in a complex magnetic structure such as that of Fig. 10, resulting in an apparently nonlocal heat transport process.

As a consequence of toroidal flux conservation during the island growth [21, 22] and $B_\varphi \approx const$, the area bounded by a helical flux surface as this evolves in time is conserved, thus $A = A(\psi_*)$. Consequently, reconnecting flux tubes mix their thermal energy density (i.e. their pressure) according to the following law

$$p[A(\psi_*)] = \pi \left[p(r_{2sp}^2) \frac{dr_{2sp}^2}{dA} - p(r_{1sp}^2) \frac{dr_{1sp}^2}{dA} \right] \qquad (3)$$

where $r_{2sp} - r_{1sp} = \xi(t)$, with r_{1sp} and r_{2sp} the radii of the two circles forming the m/n=1 island separatrix (see Fig. 10). These radii, as well as their derivatives with respect to the area, are obtained as a function of the equilibrium helical flux function, $\psi_{*eq}(r^2) \propto \int_0^{r^2} [q^{-1}(r^2) - 1] dr^2$; in particular, since surfaces with equal helical flux reconnect, $\psi_{*eq}(r_{1sp}^2) = \psi_{*eq}(r_{2sp}^2)$. In Eq. (3), we have neglected the magnetic to thermal energy transfer during reconnection, which corresponds to only a few percent of the ECH thermal energy absorbed in a sawtooth period. The plasma density obeys completely similar relations.

Thus, the temperature evolution is dominated by heating and perpendicular diffusion (a constant $\chi_\perp$ is assumed) in periods during which the m/n=1 magnetic island is either absent or has a stationary width, while convection and mixing due to reconnection become important when the island is growing, the convection pattern being associated with the specific m/n=1 internal kink mode structure. It is convenient to specify the heat transport equation in a Lagrangian frame of

reference; thus, $T = T(A,t)$. Taking into account the different topology of the three different regions, I, II and III, indicated in Fig. 10, the diffusion equation takes the form

$$\frac{3}{2}\frac{\partial T}{\partial t} = \chi_{\perp}\left(\left\langle|\nabla A|^2\right\rangle\frac{\partial^2 T}{\partial A^2} + \left\langle\nabla^2 A\right\rangle\frac{\partial T}{\partial A}\right) + \frac{\langle S\rangle}{n} \qquad (4)$$

In regions I and II the metric elements simplify: $A = \pi r^2$, with r indicating the distance from the displaced axis in region I. The time evolution of the three regions is specified by the displacement function $\xi(t)$ and by the helical flux function $\psi.\left[r, \vartheta - \varphi, \xi(t)\right]$. Equation (4), with appropriate initial and boundary conditions [21], completely specifies our simulation model.

The model was originally applied to explain the multipeaked temperature profiles and transport barriers observed in high ECH power density experiments such as RTP [23] and TEXT-U [24]. In this paper, we present two examples which indicate the model ability to reproduce the observed sawtooth shapes in TCV.

In the first example, Fig. 11, a saturated sawtooth is simulated. In this simulation, the power deposition region is set to be between about 2 cm and 4 cm from the equilibrium axis on the high field side; the q=1 radius is at 7 cm. Thus, the heating is off-axis, but is well within the q=1 radius, consistently with the experimental indications. Fig. 11 a) shows the simulated temporal trace of the local electron temperature at a distance of about 2 cm from the equilibrium magnetic axis. Frequency doubling appears in the simulation during the evolution of the saturated sawteeth, as also often seen in the experiment during saturated sawteeth [19]. In Fig. 11 b), three temperature profiles at different phases of the saturated sawtooth are shown. These profiles are non-monotonic within the mixing radius, ρ_{mix} and can become rather spiky. In Fig. 11 c), a simulated 3D reconstruction of the electron temperature corresponding to the fast relaxation phase at time $t = t_2$ of Fig. 11 a) is shown.

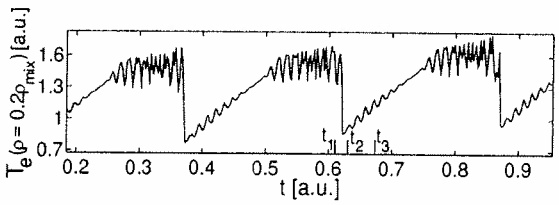

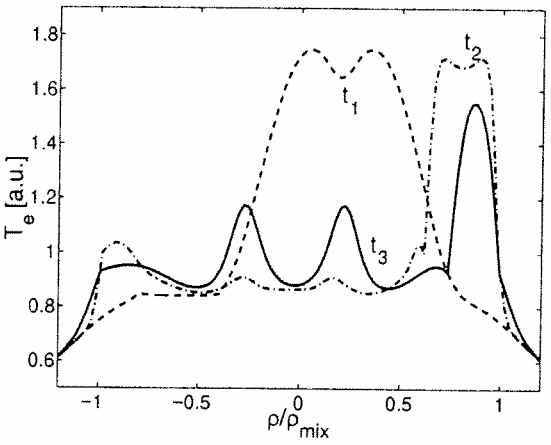

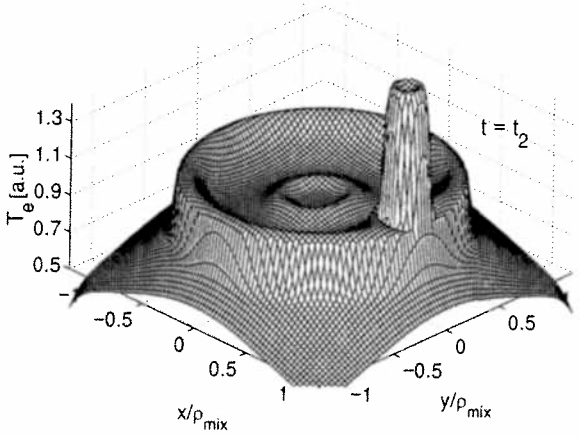

FIG. 11. Simulation of partially saturated sawteeth with power deposition between magnetic axis and the q=1 surface at ρ=0.25ρ_{mix}, with a deposition width of 0.1ρ_{mix}.

11a) temporal evolution of the central temperature. Note the appearance of frequency doubling,

11b) temperature profile before (t_1) and after crash (t_2 ,t_3), see Fig. 11 a),

11c) 3D temperature profile at time $t=t_2$, after crash.

In the second example, Fig. 12, we present the simulation of a humpback sawtooth. In order to obtain a humpback from our model, it is important to place the heating region close to the $q=1$ radius, consistently with the experiment. This produces slightly hollow temperature profiles during the quiescent phase, which then become peaked in the centre as a consequence of the growth of the $m=1$ island. Fig. 12 a) shows the temporal evolution of the central electron temperature. Temperature profiles during the fast relaxation phase are shown in Fig. 12 b). Note the relative minimum in the temperature, which deepens with time during the fast phase of the humpback relaxation. Indeed, the characteristic signature corresponding to the sudden drop in temperature between the two humps, visible in Fig. 12 a), is related to the fast passage of this relative minimum through the observation point. A 3D reconstruction of the electron temperature is shown in Fig. 12 c), clearly showing the two hot regions.

For both simulations, the displacement function, $\xi(t)$, is assumed to grow rapidly during the observed, fast relaxation phase. More specifically, for the case of the simulated saturated sawtooth, $\xi(t)$ grows from 0.2 ρ_{mix} to 0.8 ρ_{mix} in about 200 μs; for the humpback sawtooth, $\xi(t)$ grows from practically zero to 0.9 ρ_{mix} in a similar time interval. These values of $\xi(t)$ are consistent with nearly full reconnection. The typical radial width of the heat deposition region used in the simulations is between 1 and 2 cm. The results are not particularly sensitive to this width when varied within the indicated range. The typical value of the central $\chi_\perp$ used in the simulations is of order 0.1 m^2/s.

Thus, the model successfully reproduces the shapes of different types of central relaxations as the heating radius is varied, at least qualitatively speaking. In addition, consistently with the experiments, the relative amplitude of the relaxations for central versus off-axis deposition comes out correctly. For example, at constant power injection, high amplitude triangular sawteeth are obtained for on-axis heating, while low amplitude humpback oscillations are obtained when the heating region is close to the $q=1$ surface.

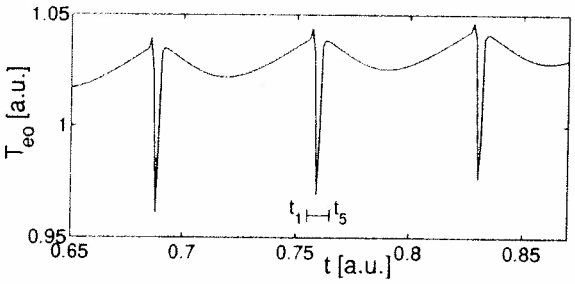

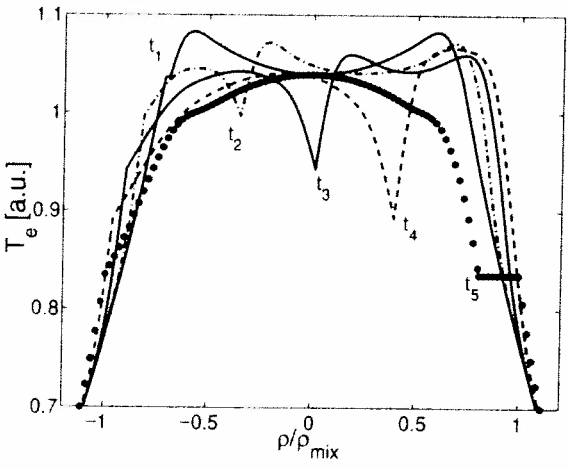

FIG. 12. Simulation of humpback sawteeth with power deposition close to $q=1$ surface:
12a) temporal evolution of the central temperature,
12b) temperature profile during the fast phase indicated in Fig. 12 a),
12c) 3D temperature profile in the middle of the crash ($t=t_3$)

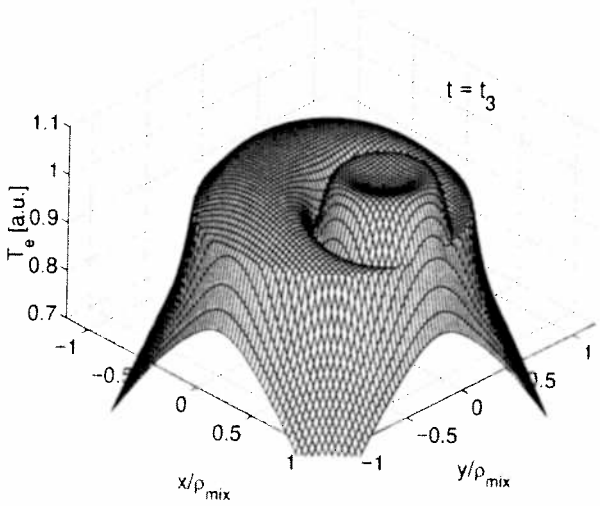

3.2 Sawtooth period simulation with localised power deposition

The transport code PRETOR (see section 2.4), including a sawtooth model developed earlier [25], had been used earlier to simulate sawtooth periods in Ohmic discharges of TCV [26]. It is now used to simulate ECR heated discharges, since it is known that temperature and density profiles are strongly influenced by the presence (or absence) of sawteeth. In particular, the strong dependence of the sawtooth period on power deposition location observed experimentally, see Fig. 13, can also be simulated.

The magnetic shear $s_1 = \rho_1 q'(\rho_1)/q_1$ at q=1 and s_{1crit}, a critical shear above which the resistive internal kink is triggered, define the time at which the sawtooth crash occurs. The sawtooth period depends on the relative time evolution of s_1 and s_{1crit}, and therefore mainly on the local plasma parameters. This explains why the sawtooth activity is very sensitive to localised ECRH power deposition, as seen for example in TCV [18]. Indeed, local heating can change both $s_1(t)$, by changing the local resistive time and the current profile, and $s_{1crit}(t)$ by changing the temperature gradients and confinement time. Moreover, localised deposition affects the q=1 radius both in the transport code and in the experiment, as revealed by measurements of the sawtooth inversion radius. We have simulated a case with 0.5 MW of ECRH deposited over a radial width of 0.15 a. Changing the mean deposition radius from ρ = 0 to 0.3 to 0.5, the code gives ρ_1/a = 0.44, 0.40 and 0.27 respectively. In addition, in the first two cases, s_{1crit} is relatively large, 0.35, because heating inside q=1 gives large gradients at q=1. Therefore long sawtooth periods are obtained, as shown in Fig. 14 (ρ_{ECRH}=0.3). On the contrary, heating outside ρ_1 gives a relatively smaller s_{1crit} and therefore short sawtooth periods are obtained (ρ_{ECRH}=0.4 in Fig. 14). This is in qualitative agreement with the experiment, where sawtooth periods of 2 ms are observed when heating outside q=1 and where sawtooth periods are seen to increase rapidly to 7-8 ms when heating approaches the q=1 surface. However, in the experiment, heating closer to the magnetic axis results again in shorter sawtooth period; this indicates that a more detailed simulation including the magnetic topology described in above section 3.1.2, is needed when heating inside the reconnecting volume.

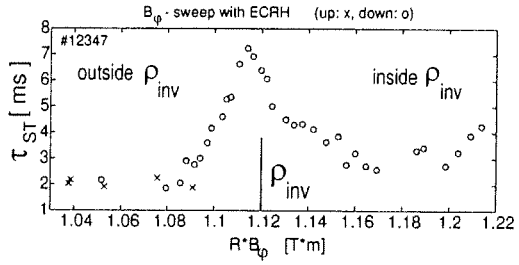

FIG. 13. Sawtooth period evolution during a power deposition sweep (toroidal magnetic field sweep). Maximum sawtooth period is observed for close to ρ_{inv} deposition

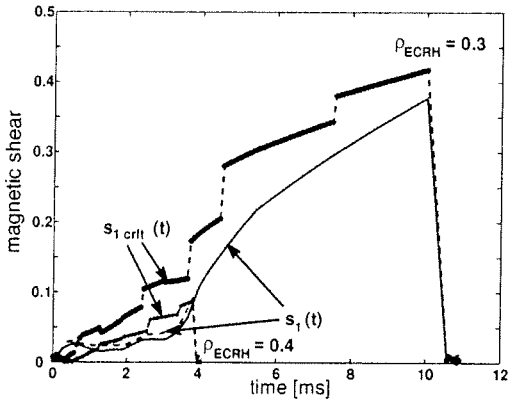

FIG. 14. Evolution of the local magnetic shear s_1 (red) and critical magnetic shear s_{1crit} (blue), for power deposition 1) close to q=1, resulting in long sawtooth period (ρ_{ECRH}=0.3, solid lines), 2) outside q=1, resulting in shorter sawtooth period (ρ_{ECRH}=0.4, dashed lines).

4. CONCLUSIONS

The electron energy confinement has been studied as a function of plasma shape, i.e. as a function of elongation and triangularity in EC heated discharges, with P_{EC} exceeding P_{OH} by up to an order of magnitude. The electron energy confinement improves with elongation. The beneficial effect of low or negative triangularity on confinement, manifested in Ohmic plasmas, is also observed in EC heated plasmas, but tends to decrease with increasing power. Results of transport simulations, using two different models, are found to be consistent with the experimental data.

A variety of different types of central relaxations (sawteeth) are observed when the location of power deposition is moved from the magnetic axis to the q=1 region. The observed sawtooth shapes have been qualitatively simulated, using a model with localised power deposition, a growing (convection and reconnection) and rotating island at q=1, and finite thermal diffusivity across field lines. Sawtooth shapes similar to those observed in the experiment are reproduced when the power deposition location is moved from the magnetic axis to the q=1 region.

The observation that the sawtooth period is maximum when the power is deposited close to the q=1 surface has also been reproduced by simulation. The model simulates the evolution of the local magnetic shear and includes a critical shear above which the resistive internal kink is triggered.

The improved understanding of sawtooth behaviour may lead to the capability of controlling sawteeth in tokamaks.

5. ACKNOWLEDGEMENTS

This work was partly supported by the Fonds National Suisse de la Recherche Scientifique

REFERENCES

[1] CORDEY, J.G. et al., Plasma Phys. Controlled Fusion **39**, B115 (1997).
[2] THOMSEN, K. et al., 17th IAEA Fusion Energy Conference, Yokohama 1998, Paper CN-69/ITER/3-ITER P1/07.
[3] MARTIN, Y. and SAUTER, O., Considerations on Energy Confinement Time Scalings using present Tokamak Databases and Prediction for ITER Size Experiments, CRPP Lausanne Report LRP 616/98, to be submitted to Nuclear Fusion.
[4] MILLER, R.L. et al., Phys. Rev. Lett. **43**, (1979) 765.
[5] TROYON, F. et al., Plasma Phys. Controlled Fusion **26**, (1984) 209.
[6] HOFMANN, F. et al., Phys. Rev. Lett. **81**, 2918 (1998).
[7] LAZARUS, E.A. et al., Phys. Fluids **B 3** (1991) 2220.
[8] GOODMAN, T.P. et al., 19th Symp. on Fusion Technology, Lisbon, 1996, Vol. **I**, 565.
[9] GOODMAN, T.P. et al., presented by M.Q. TRAN. Invited Paper, 3rd Int. Workshop on Strong Microwaves in Plasmas, Russia, August 1996, ed. by A.G. Litvak, Nizhny Novgorod Univ. Press 1997.
[10] WEISEN, H. et al., Plasma Phys. Control. Fusion **40** (1998) 1803.
[11] POCHELON, A. et al., Proc. of Joint ICPP 1998 and 25th EPS Conf. on Contr. Fusion and Plasma Physics, Praha 1998, ECA Vol. **22C** (1998) 1324.
[12] WEISEN, H. et al., Nuclear Fusion **37** (1997) 1741.
[13] MORET, J-M., et al., Phys. Rev. Lett. **79** (1997) 2057.
[14] REBUT, P.H., LALLIA, P.P. and WATKINS, M.L., Proc. 12th Int. Conf. Plasma Physics and Controlled Nuclear Fusion Research, Nice 1988, IAEA Vienna 1989, Vol. **2**, 191.
[15] BOUCHER, D. and REBUT, P.H., in Proc. IAEA Tech. Committee on Advances in Simulation and model. of Thermonuclear plasmas, 1992, Montreal (1993) 142.
[16] ANGIONI, C. et al., Proc. of the Joint Varenna-Lausanne Int. Workshop on Theory of Fusion Plasmas, 18th Int. School of Plasma Physics, Aug. 31st - Sept. 4th 1998, Varenna, Italy, ed. by J.W. Connor, E. Sindoni and J. Vaclavik, Societa Italiana di Fisica, Bologna, Editrice Compositori, Bologna, Italy, ISSP-18 (1999) 493; CRPP Report LRP 617/98.
[17] DNESTROVSKII, Y.N. et al., Plasma Phys. Reports, **23** (1997), (transl. from Fizika Plazmy).
[18] PIETRZYK, Z.A. et al., accepted for publication in Nuclear Fusion, and PIETRZYK, Z.A. et Proc. of Joint ICPP 1998 and 25th EPS Conf. on Contr. Fusion and Plasma Physics, Praha 1998, ECA Vol. **22C** (1998) 1328.
[19] POCHELON, A. et al., Proc. of 24th EPS Conf. on Controlled Fusion and Plasma Physics, Berchtesgaden 1997, Vol. **21A**, Part II (1997) 537.
[20] KISLOV, D.A. et al., 22nd EPS Conf. on Contr. Fus. and Plasma Phys., Vol. **19C**, Part I (1995) 369 and RAZUMOVA, K.A. et al., Plasma Physics Reports **23** (1997) 13.
[21] PORCELLI, F., ROSSI, E. et al., Phys. Rev. Lett. **82** (1999) 1458.
[22] KADOMTSEV, B. B., Fizika Plazmy **1**, 710 (1975) (Sov. J. Plasma Phys. **1**, 389 (1975)).
[23] LOPES CARDOZO, N.J. et al., Phys. Rev. Lett. **73**, (1994) 256.
[24] CIMA, G. et al., Plasma Physics and Controlled Fusion **40** (1998) 1149.
[25] PORCELLI, F. et al., Plasma Phys. Contr. Fusion **38** (1996) 2163.
[26] SAUTER, O., ANGIONI, C. et al., Proc. of the Joint Varenna-Lausanne Int. Workshop on Theory of Fusion Plasmas, 18th Int. School of Plasma Physics, Aug. 31st - Sept. 4th 1998, Varenna, Italy, ed. by J.W. Connor, E. Sindoni and J. Vaclavik, Societa Italiana di Fisica, Bologna, Editrice Compositori, Bologna, Italy, ISSP-18 (1999) 403; or CRPP Report LRP 617/98.